

# **A combined RNA-seq and whole genome sequencing approach for identification of non-coding pathogenic variants in single families.**

5

6 Revital Bronstein,<sup>1</sup> Elizabeth E. Capowski,<sup>2</sup> Sudeep Mehrotra,<sup>1</sup> Alex D. Jansen,<sup>2</sup>  
7 Daniel Navarro-Gomez,<sup>1</sup> Mathew Maher,<sup>1</sup> Emily Place,<sup>1</sup> Riccardo Sangermano,<sup>1</sup>  
8 Kinga M.Bujakowska,<sup>1</sup> David M. Gamm,<sup>3</sup> Eric A. Pierce,<sup>1\*</sup>.

9

10 1. Ocular Genomics Institute, Massachusetts Eye and Ear Infirmary, Harvard  
11 Medical School, Boston, MA, 02114, USA.

12 2. University of Wisconsin-Madison, Waisman Center Stem Cell Research  
13 Program, Madison, WI, 53705, USA.

14 3. Department of Ophthalmology and Visual Sciences, University of Wisconsin-  
15 Madison, McPherson Eye Research Institute, Waisman Center Stem Cell  
16 Research Program, Madison, WI, 53705, USA.

17 \*Correspondence: [eric\\_pierce@meei.harvard.edu](mailto:eric_pierce@meei.harvard.edu)

18

# 19 Abstract

20 Inherited retinal degenerations (IRDs) are at the focus of current genetic  
 21 therapeutic advancements. For a genetic treatment such as gene therapy to be  
 22 successful an accurate genetic diagnostic is required. Genetic diagnostics relies  
 23 on the assessment of the probability that a given DNA variant is pathogenic.  
 24 Non-coding variants present a unique challenge for such assessments as  
 25 compared to coding variants. For one, non-coding variants are present at much  
 26 higher number in the genome than coding variants. In addition, our  
 27 understanding of the rules that govern the non-coding regions of the genome is  
 28 less complete than our understanding of the coding regions. Methods that allow  
 29 for both the identification of candidate non-coding pathogenic variants and their  
 30 functional validation may help overcome these caveats allowing for a greater  
 31 number of patients to benefit from advancements in genetic therapeutics. We  
 32 present here an unbiased approach combining whole genome sequencing  
 33 (WGS) with patient induced pluripotent stem cell (iPSC) derived retinal organoids  
 34 (ROs) transcriptome analysis. With this approach we identified and functionally  
 35 validated a novel pathogenic non-coding variant in a small family with a  
 36 previously unresolved genetic diagnosis.

37

## 38 Introduction

39 Inherited retinal degenerations (IRDs) are a leading cause of blindness,  
 40 altogether affecting >2million people worldwide. IRDs are characterized by  
 41 progressive degeneration of photoreceptor and/or retinal pigment epithelial  
 42 (RPE) cells of the retina with variable age of onset and rates of degeneration<sup>1</sup>.  
 43 Despite tremendous ongoing efforts and research into various therapeutics,  
 44 treatments for IRDs remain limited. Currently there are two regulatory agency-  
 45 approved treatment approaches, retinal prosthesis implants and gene  
 46 augmentation therapy for IRD caused by mutations in the *RPE65* gene<sup>1-7</sup>. The  
 47 eye is a prime candidate for gene therapy approaches due to its relative immune-  
 48 privilege, surgical accessibility and ease of non-invasive monitoring. In addition,  
 49 IRDs are Mendelian disorders caused by mutations in single genes in the vast  
 50 majority of cases. Owing to these favorable circumstances several gene/genetic  
 51 therapy clinical trials have been initiated for IRDs, including those caused by  
 52 mutations in the *ABCA4*, *CEP290*, *CHM*, *CNGA3*, *CNGB3*, *MYO7A*, *RPGR*,  
 53 *RS1*, and *USH2A*<sup>6</sup>.

54 As each genetic therapy targets a specific gene, for a patient to be considered for  
 55 treatment they must obtain a reliable genetic diagnosis. Difficulties inherent to  
 56 genetic diagnostics are rooted in the fact that every individual carries millions of  
 57 DNA variants in their genome<sup>8,9</sup>. The large majority of the DNA variants are  
 58 found in non-coding regions of the genome such as intergenic and intronic  
 59 regions. Since non-coding sequences can better tolerate sequence variation

compared to coding sequences, most of these variants are benign and do not lead to disease. Still, some non-coding variants are found to be pathogenic by altering gene expression and/or splicing patterns<sup>10–12</sup>. As a result, non-coding variants are among the hardest to classify and thus under-diagnosed<sup>13,14</sup>. Algorithms exist that predict the effect of a non-coding variant on gene expression or splicing based on analysis of the DNA sequence alone, but their accuracy for diagnostic purposes remains undetermined<sup>15–18</sup>.

In order to functionally test the effects of non-coding variants one needs to quantify the level of gene expression and analyze the splicing patterns of the presumably affected genes. When multiple variants in multiple genes need to be evaluated, advanced methods for whole transcriptome analysis are advantageous. Indeed, previous studies successfully utilized large RNA-seq datasets from tissue biopsies to identify novel non-coding pathogenic variants<sup>19,20</sup>. For example, Evrony *et al* narrowed down a linkage analysis in a very large pedigree to a single non-coding variant using RNA-seq. This non-coding variant was shown to cause intron retention in the *DONSON* gene and is most likely the genetic cause of microcephaly-micromelia syndrome (MMS) in this population<sup>19</sup>. Cummings *et al* used 184 skeletal muscle RNA-seq samples available through Genotype-Tissue Expression resource (GTEx)<sup>21</sup> as a reference panel for 50 patients with undiagnosed muscle disorders. This comparison led to a genetic diagnosis for 17 previously unsolved families and identification of several splice altering variants<sup>20</sup>.

Such studies depend on the availability of large, publicly available RNA-seq datasets and/or on a large cohort of patients. They also require biopsy samples from a clinically relevant tissue or cell type. Both gene expression and splicing are tissue-specific<sup>22,23</sup> owing to restricted availability of transcription and splicing factors with variable usage of regulatory DNA sequences<sup>24–27</sup>. Consequently, DNA variants in such regulatory sequences can have tissue-specific outcomes on gene expression and splicing<sup>18,28</sup>. Thus, analyzing RNA from a clinically relevant tissue or cell type is crucial to obtain a more focused and reliable diagnostic result. When a clinically relevant tissue is not accessible, *ex vivo* surrogate models can sometimes suffice. Indeed, a study aimed at discerning the genetic causality of patients with monogenetic neuromuscular disorders found that t-myotubes, skeletal myotubes derived by myoD overexpression in fibroblasts, accurately reflected the muscle transcriptome and faithfully revealed pathogenic variants<sup>29</sup>.

In this study, we aimed to develop a pipeline that would detect putative non-coding pathogenic mutations in a small family. We present a pilot study performed in a five member family with two siblings affected by cone dysfunction syndrome in which we successfully identify and functionally validate a novel deep intronic variant without the use of large reference datasets. Obtaining a clinically relevant tissue from IRD patients is not possible as the retina cannot be safely biopsied. To overcome this limitation, we have made use of patient-derived induced pluripotent stem cells (iPSCs) that were differentiated *in vitro* to form retinal organoids (ROs)<sup>30</sup>. ROs have been shown to recapitulate many aspects of

human retinal structure and function<sup>30,31,40,32–39</sup>. We show that the RO transcriptome is much closer to the transcriptome of normal human retina than other more readily available diagnostic tissues. More importantly, we show for the first time that analysis of a patient-derived RO transcriptome can successfully detect pathogenic deep intronic variants that activate cryptic splice sites, leading to a new genetic diagnosis. Our approach can lead to a larger number of patients to be eligible for genetic therapies.

## Materials and Methods

### Human Subjects

The study was approved by the institutional review board at the Massachusetts Eye and Ear (Human Studies Committee MEE in USA) and adhered to the Declaration of Helsinki. Informed consent was obtained from all individuals on whom genetic testing and further molecular evaluations were performed.

### Pluripotent Stem Cell Induction

Tissue samples were obtained with written informed consent in adherence with the Declaration of Helsinki and with approval from institutional review boards at the University of Wisconsin-Madison and Massachusetts Eye and Ear Infirmary. Blood samples from 4 individuals from family OGI-081 (197, 198, 200 and 340) were collected and reprogrammed by Cellular Dynamics, Inc (now FUJIFILM Cellular Dynamics, Inc) as custom MyCell products. Three independent clones from each individual were karyotypically normal, expressed pluripotency markers and successfully differentiated to retinal organoids (<sup>41</sup>: lines 1579, 1580, 1581

and 1582). Stem cells were maintained on Matrigel (ThermoFisher) in either mTeSR1 (WiCell) or Stemflex (ThermoFisher) and passaged with either Versene or ReLeSR (STEMCELL Technologies).

### Retinal Organoid (RO) Differentiation

Differentiation of iPSCs was performed as previously described<sup>41</sup>. Briefly, embryoid bodies (EB) were lifted with either 2 mg/ml dispase or ReLeSR and weaned into Neural Induction Media (NIM: DMEM:F12 1:1, 1% N2 supplement, 1x MEM nonessential amino acids (MEM NEAA), 1x GlutaMAX and 2 mg/ml heparin (Sigma)) over the course of 4 days. On day 6, 1.5 nM BMP4 (R&D Systems) was added to fresh NIM and on day 7, EBs were plated on Matrigel at a density of 200 EBs per well of a 6-well plate. Half the media was replaced with fresh NIM on days 9, 12 and 15 to gradually dilute the BMP4 and on day16, the media was changed to Retinal Differentiation Media (RDM: DMEM:F12 3:1, 2% B27 supplement, MEM NEAA, 1X antibiotic, anti-mycotic and 1x GlutaMAX). On days 25-30, optic vesicle-like structures were manually dissected and maintained as free floating organoids in poly HEMA (Sigma)- coated flasks with twice weekly feeding of 3D-RDM (RDM + 5% FBS (WiCell), 100  $\mu$ M taurine (Sigma) and 1:1000 chemically defined lipid supplement) to which 1  $\mu$ M all-trans retinoic acid (Sigma) was added until d100. Live cultures were imaged on a Nikon Ts2-FL equipped with a DS-fi3 camera.

### Immunocytochemistry and Microscopy

Organoids were fixed in 4% paraformaldehyde at room temperature for 40 min, cryopreserved in 15% sucrose followed by equilibration in 30% sucrose, and

sectioned on a cryostat. Sections were blocked for 1 hr at room temperature (RT) in 10% normal donkey serum, 5% BSA, 1% fish gelatin and 0.5% Triton then incubated overnight at 4°C with primary antibodies diluted in block. Table S1 lists primary antibodies, dilutions and sources. Slides were incubated with species-specific fluorophore-conjugated secondary antibodies diluted 1:500 in block, for 30 minutes in the dark at RT (Alexa Fluor 488, AF546 and AF647). Sections were imaged on a Nikon A1R-HD laser scanning confocal microscope (Nikon Corporation, Tokyo, Japan).

#### DNA Sequencing

DNA was extracted from venous blood using the DNeasy Blood and Tissue Kit (Qiagen, Hilden, Germany). OGI-081-197 underwent GEDi sequencing as described previously<sup>42</sup>. All five family members underwent whole exome and PCR-free whole genome sequencing. Sequencing was done at the Genomics Core at Massachussets Eye and Ear as described previously<sup>43</sup>.

#### RNA Sequencing

For transcriptome analysis, ROs from at least 2 different clones per individual were harvested at approximately day160 (early stage 3), lysed in 350 µl buffer RLT+ME from the RNeasy mini kit (Qiagen), snap frozen on dry ice and stored at -80C. At a later time samples were defrosted on ice and passed through QIAshredder columns (Qiagen). Subsequently, Total RNA was extracted per the manufacturer's instructions. RNA quality and quantity was assessed on an Agilent 2100 Bioanalyzer, RIN number ranged between 9.6-9.9. For each sample 1µg of total RNA spiked with 1.2ng Sequins (v2) controls<sup>44</sup> was used to generate



RNA-seq paired-end libraries with the Illumina TruSeq Stranded Total RNA kit. Ribosomal RNA was removed with the Ribo-Zero Human/Mouse/Rat kit. Libraries were multiplexed and sequenced on an Illumina HiSeq 2500 instrument for 101 cycles.

## Bioinformatics

Whole exome sequence data was analyzed in house<sup>43</sup> and whole genome data was analyzed in collaboration with the Broad Institute of MIT and Harvard using methodology described previously<sup>20</sup>. Briefly, BWA was used for alignment. GATK was used for single nucleotide polymorphism and insertion/deletion calls. Additional variant annotation was performed using the Variant Effect Predictor (VEP)<sup>45</sup>. Variants of interest were limited to polymorphisms with less than 0.005 allelic frequency in the gnomAD and ExAC databases<sup>8,9</sup>. Whole genome copy number analysis, with consideration of structural changes, was done using Genome STRiP 2.0<sup>46</sup>.

For analyses of RNA-seq data, read quality was assessed with FastQC v0.11.3 (Babraham Bioinformatics, Cambridge, UK) and MultiQC v1.2<sup>47</sup>. Reads were aligned to the human genome version GRCh37 by the STAR v2.5.3a<sup>48</sup> aligner in two-pass mode within the sample and across replicates for each sample sets. Annotations were derived from the Human GENCODE v19 (Ensemble74).

FeatureCount v1.5.2<sup>49</sup> from the Subread package, was used to generate gene expression matrix with the following non-default settings, reads must be paired, both the pairs must be mapped, use only uniquely mapped reads, multi-mapped reads are not counted, chimeric reads are not counted and strand specificity

turned on. Anaquin<sup>50</sup> was further used to evaluate alignment sensitivity and gene expression. Here sensitivity indicates the fraction of annotated regions covered by alignments of the reads by STAR (Table S2). No limit of quantification or limit of detection was reported.

For discovery of novel or known alternative splicing events we used a combination of CASH v2.2.1<sup>51</sup> and MAJIQ v1.1.3a<sup>52</sup>. CASH was operated with default settings. MAJIQ was run with a minimum of 5 reads for junction detection and 10 reads for the calculation of delta percent spliced-in (dPSI). EdgeR (v3.2.2)<sup>53</sup> was used to perform differential gene expression with default settings. Data normalization was performed using trimmed mean of M-values (TMM).

Next, the raw read counts were converted to transcript per million (TPM) expression values. The Picard tools v1.87 and RSeQC v2.6.4<sup>54</sup> were used to calculate mean fragment length. The approach implemented in Kallisto<sup>55</sup> was used to convert raw reads to TPM values. An average TPM of the third lowest Sequins between test and control samples was calculated and used as cutoff.

TPM values for the GTEx samples used in figure3 were downloaded from the GTEx portal. The human normal retina (HNR) samples<sup>56</sup> and the ENCODE skin samples were reanalyzed as described above. The ENCODE skin samples were used for the analysis performed with MAJIQ as they were generated with a stranded total RNA-seq library same as our RO samples. In contrast the GTEx samples were generated with an mRNA non-stranded library.

## RT-PCR and cloning

RT-PCR was conducted using SuperScript IV first-Strand synthesis system (ThermoFisher Scientific, Waltham, MA). Exon 14b was amplified with primers F: GACATGTTGCTAAGATTGAAATCCGT from exon 14 and R: GACCCAGCTTTCAGAGTAACCAGAAC from exon 15 using Phusion polymerase (NEB, Ipswich, MA). The longer band containing exon14b was then excised from the gel and purified using Zymoclean gel DNA recovery kit (Zymoresearch, Irvine, CA) and cloned using pGEM-T Easy Vector System (Promega, Madison, WI). The plasmid was used in a transformation into Subcloning Efficiency DH5α Competent Cells (Invitrogen, Carlsbad, CA). The plasmid was isolated with Zyppy Plasmid Miniprep Kit (Zymoresearch, Irvine, CA). All procedures described in this section were conducted according to the manufacturer instructions. The DNA sequence of Exon 14b was found to be:

GCCAGGTGCAGTGGCTCACGACTGTAATTCCAACACTTTGGGAGGCCAAGG  
TGGCAGGATCACATAAGTCCAGGAGTTCAAGACAAGCCTGGACAACATG.

## Results

### Unresolved genetic analysis of family OGI-081

The pilot study reported here was conducted on a five member family with two siblings shown by clinical testing to be affected by a cone dysfunction syndrome (Figure1a). Both affected patients had nystagmus and decreased vision from infancy and at age 8, OGI-081-197 was also noted to have photophobia. Visual acuity for both affected patients measured 20/150-200 and remained stable for 3 years. Full field electroretinogram (ffERG) testing of retinal function for OGI-081-197 was significant for reduced and delayed cone photoreceptor responses, with normal rod photoreceptor response amplitudes. Optical coherence tomography (OCT) imaging of the retina showed retinal degenerative changes in the fovea (Figure1b). In addition to their retinal disease, both affected patients were found to have Chiari malformations. Interestingly, vision phenotypes such as photophobia, vision loss and nystagmus have been reported as accompanying symptoms in some forms of Chiari malformations<sup>57-60</sup>. Unfortunately, despite evidence that Chiari malformations have a heritable component<sup>61-63</sup>, the genes involved are not yet well defined<sup>59,64,65</sup>. For that reason we could not rule out the possibility that the vision phenotypes and Chiari malformations share a common genetic causality.

The phenotypes segregation in OGI-081 is indicative of a recessive mode of inheritance. Thus, for genetic testing we searched for genes that have putatively pathogenic variants in both alleles (Figure1a). Selective exon capture based

genetic diagnostic testing was performed using the Genetic Eye Disease (GEDi) test<sup>42</sup>. Since this did not identify a clear cause of disease, whole exome sequencing (WES) for the five members of the family was performed. Both the GEDi testing and WES identified a single rare variant in the *CNGB3* gene (c.1148delC, p.Thr383IlefsTer13) which has been reported to be pathogenic<sup>66–68</sup>, but a second rare variant in *CNGB3* was not identified, nor were other potential causative genetic variants forthcoming for the two affected members of the family. *CNGB3* mutations are among the most common causes of cone dysfunction syndrome, but to the best of our knowledge, Chiari malformations have not been reported as an accompanying symptom in *CNGB3* patients<sup>69,70</sup>. Moreover, the  $1.75 \times 10^{-3}$  gnomAD allele frequency of the p.Thr383IlefsTer13 variant is higher than expected for recessive pathogenic variants and two homozygous individuals are reported in the gnomAD database. Since it has been proposed that up to 1 in 4-5 individuals in the general population may be a carrier of null mutations in IRD genes<sup>71</sup> it was possible that the presence of variant p.Thr383IlefsTer13 was an incidental finding.

We therefore decided to test for two possible disease scenarios. One is that *CNGB3* accounts for the cone dysfunction syndrome and the second allele is a non-coding variant. In this case the Chiari malformation has a separate, unrelated causality. The second possibility is that a novel disease-causing gene is responsible for both the cone dysfunction syndrome and the Chiari malformation. To test these hypotheses, we performed both whole genome sequencing (WGS) and RNA-seq analysis of a surrogate retinal tissue to

determine whether the combination of these orthogonal investigations could yield a clear genetic solution.

Analysis of DNA variants detected by WGS identified 3268 segregating rare variants that could be sorted into 8191 allelic pairs in 642 genes (TableS3). The variant ranked at the top of the list of potential causes of disease remained the known pathogenic variant c.1148delC; p.Thr383IlefsTer13 in the *CNGB3* gene. However, a second coding variant once again was not found in this gene. Next, we set to establish a clinically relevant surrogate transcriptome for the human retina.

The iPSC-derived retinal organoid (RO) transcriptome can be used as a surrogate for a human retinal biopsy

Patient-derived iPSCs were generated from peripheral blood monocytes of all members of family OGI-081 excluding OGI-081-199. The iPSCs were subjected to an *in vitro* differentiation process to generate ROs with attached RPE (Figure 2a)<sup>30</sup>. RPE was specifically retained in the ROs so as to concurrently identify potential mutations in RPE genes as well as photoreceptor genes (Figure2b). The ROs were kept in culture for 160 days (early stage 3<sup>30</sup>), a time point at which outer segments are visible by light microscopy and cone and rod cells are clearly distinguished by immunocytochemistry (Figure2b, c-h). At da160, ROs were harvested for total RNA isolation, library preparation, and RNA-seq analysis (Table1).

In order to evaluate if day 160 ROs can be used as informative surrogates for the adult human retinal transcriptome, we examined the expression levels of 270 known IRD genes reported in the RetNet database. For this analysis, we compared an in-house dataset composed of 3 post-mortem human normal retinas (HNR, N=3)<sup>56</sup> to ROs derived from the unaffected sibling (N=5) or skin or whole blood samples taken from the GTEx database (Figure 3 and Table S4)<sup>21</sup>. Skin and blood represent tissues that are more readily available – and thus commonly used – for surrogate diagnostic testing. We found 224 IRD genes to be expressed in HNR (TPM>1). Interestingly we were able to detect expression of 254 IRD disease genes in the RO samples (Figure 3 and TableS4). The higher detection rate of disease-causing genes in ROs compared to HNR is most likely because of overall higher TPM values in RO samples (Figure 3a&b), possibly due to higher RNA quality compared to post-mortem HNR samples. In addition, the presence of RPE and photoreceptors with varied maturation statuses in the RO samples could be contributing factors to this finding. As expected, skin and blood expressed lower numbers of IRD genes (188 & 130 respectively) at much lower TPM values (Figure 3a&b and Table S4). Since IRD genes were very poorly represented in the blood samples, we excluded blood from further analysis.

We next examined the complexity of the HNR, RO and skin transcriptomes, which is reflected by the multitude of isoforms that are produced from each gene locus<sup>72,73</sup>. Isoform diversity that occurs via alternative splicing of the pre-mRNA can be represented by the splice junctions detected in each gene locus. We used

the MAJIQ<sup>52</sup> algorithm to detect splice junctions in HNR and RO samples of the OGI-081 unaffected sibling, and the ENCODE database<sup>74,75</sup> to detect splice junctions in corresponding skin samples. The skin samples from the ENCODE database were more suited for this analysis than the GTEx samples due to RNA-seq library type (see Materials and Methods). We found a comparable number of splice junctions in the HNR and RO samples (41,121 and 31,535 (76%) respectively) but a much lower number in the skin samples (16,713 (40%)) (Figure 3c and TableS5). This result is probably due to the fact that HNR and ROs are composed of a more diverse cell population than skin. More importantly, in IRD genes, the gap in complexity between the HNR (946 junctions) and ROs (739 (78%)) as compared to skin (227(24%)) is even greater (Figure 3d & Table S5). Thus, the RO transcriptome provided a close facsimile of the human retinal and IRD transcriptomes at the gene expression and splicing pattern levels, whereas the skin transcriptome did not.

### Detection of a novel non-coding pathogenic variant in *CNGB3*

In order to find the underlying genetic cause of the retinal degeneration in OGI-081 affected patients, we conducted differential splicing and gene expression analyses of the RNA-seq data obtained from day 160 ROs of affected versus unaffected siblings. The differential splicing analysis was conducted with CASH<sup>51</sup> and MAJIQ<sup>52</sup> algorithms, and we used edgeR algorithm<sup>53</sup> for differential gene expression. CASH detected 106 differential splicing events in 101 genes (Table S6), while MAJIQ detected 522 differential splicing junctions in 260 genes (Table S7). A comparison to the 642 genes with DNA variant pairs indicated that only



two genes, *CNGB3* and *NCALD*, had altered splicing patterns and a DNA variant in each of their alleles that segregated according to disease status in OGI-081 (Figure 4a).

For the *NCALD* gene, the alternative splicing events identified by CASH and MAJIQ were isoform switching events between minor isoforms (data not shown) whose biological significances are unclear. In addition, the DNA variants in this gene are located 15-50kb away from the nearest alternative junction (Figure 4b and Table S8). Given such large distances, it is not likely that these variants could cause the alternative splicing events. Moreover, the differential gene expression analysis did not find the *NCALD* gene to be differentially expressed between the affected and unaffected siblings (Table S9). Taken together, these results indicate that the *NCALD* gene variants are most likely not the genetic cause for the disease phenotypes observed in OGI-081.

We next examined the *CNGB3* gene locus. Based on segregation in the family, we found one allele carrying the intronic variant chr8:g.87618576G>A while the second allele carried the known pathogenic variant c.1148delC; p.Thr383IlefsTer13, and a second intronic variant chr8:g.87676221T>C (Table S3). Both MAJIQ and CASH detected an alternative splicing event spanning variant chr8:g.87618576G>A. In contrast, no alternative splicing events were found to span variant chr8:g.87676221T>C (Figure 4b and Table S6-8). Close examination of the alternative splicing event spanning variant chr8:g.87618576G>A revealed that it incorporated a cryptic exon into *CNGB3* in RNA samples taken from both affected siblings but not from the unaffected

sibling (Figure 5a&b). The cryptic exon is spliced between canonical exon 14 and exon 15 and will therefore be termed exon14b from hereon. The inclusion of exon 14b was validated by RT-PCR and subsequent cloning and Sanger sequencing of the novel longer isoform from the two affected siblings (Figure 5b).

Both the addition of exon 14b to the *CNGB3* transcript as a result of variant chr8:g.87618576G>A, and the single base pair deletion in the second allele carrying variant c.1148delC; p.Thr383IlefsTer13, lead to a frame shift and subsequent premature termination. We therefore expected both alleles to undergo nonsense mediated decay (NMD) with down regulation of *CNGB3* mRNA levels in the affected siblings as compared to the unaffected sibling. However, contrary to our expectations, *CNGB3* expression was not significantly down regulated in our RNA-seq dataset, as analyzed using the edgeR program. A comparison of each of the affected siblings with the unaffected sibling yielded log<sub>2</sub>FC values of -1.05 and -1.13, indicating slightly lower expression levels in the affected siblings that did not reach statistical significance (p-values of 0.13 and 0.16 respectively (Table S9)). These two frame shift alleles are predicted to encode truncated proteins. The protein encoded by the exon 14b including isoform is predicted to maintaining a full transmembrane domain but lack the ligand binding domain of *CNGB3* (Figure 5c). Similarly, the protein encoded by the isoform carrying the known pathogenic variant c.1148delC; p.Thr383IlefsTer13 is predicted to have a truncated transmembrane domain in addition to lacking the ligand binding domain (Figure 5c). In order to determine whether the truncated *CNGB3* proteins are being translated, we performed

immunohistochemistry on ROs from the exon 14b allele carrier parent (OGI-081-200) and one affected sibling (OGI-081-197, Figure 6). CNGB3 is a subunit of the cone cyclic nucleotide-gated (CNG) channel, which localizes to cone photoreceptor outer segments in chicken and mice<sup>76,77</sup>. We have also validated the localization of human CNGB3 to cone photoreceptor outer segments in the human retina (Figure S2). We therefore immunostained ROs for CNGB3 and ML opsin, the latter serving as a marker for photoreceptor outer segments. For these studies, stage 3 ROs were kept in culture for a total of 262 days, allowing cones full opportunity to mature and localize ML opsin and CNGB3 to the photoreceptor outer segments. As expected, CNGB3 co-localized with ML opsin in cone photoreceptor outer segments in the parent (Figure 6c), with weaker staining observed in inner segments as well (Figure 6b&c), presumably due to mislocalization of truncated CNGB3 protein produced by the exon 14b including allele. In ROs from the affected sibling, where both alleles are predicted to result in truncated proteins, CNGB3 was only observed diffusely in the cell body and in inner segments; i.e., no co-localization with ML opsin was observed in cone photoreceptor outer segments (Figure 6e&f). Taken together, results from the differential splicing analysis indicate that the likely cause for the inherited retinal degeneration in OGI-081 is two pathogenic alleles in *CNGB3* - the known pathogenic allele p.Thr383IlefsTer13 and the novel deep intronic allele chr8:g.87618576G>A; NM\_019098.3:c.1663 – 2137C>T; pLeu524 IlefsTer50.

## Splicing prediction algorithms

With the identification of the non-coding pathogenic variant in *CNGB3*, we set out to examine the mechanism by which it promotes the inclusion of exon 14b. We analyzed the splice junctions surrounding exon14b with the variant analysis tool Alamut Visual. Alamut Visual incorporates three splicing predictors capable of analyzing deep intronic variants, SpliceSiteFinder-like (SSF)<sup>78</sup>, MaxEntScan<sup>79</sup> and NNSPLICE<sup>80</sup>. All three algorithms predicted chr8:g.87618576G>A to strengthen a cryptic donor splice site (DSS) (Table 2). All three algorithms also detected a potential acceptor splice site (ASS) at position c.1663-2238, exactly where our Sanger sequencing indicated the acceptor site of exon 14b resides. Interestingly, exon 14b ASS is a stronger than the one located at exon 15 (Table 2). It is plausible that the availability of this acceptor site and its ability to compete with the acceptor site of exon 15 contributed to the effect of variant chr8:g.87618576G>A on the splicing pattern of *CNGB3* in the affected siblings. In addition we noticed the presence of a second even stronger alternative ASS 54bp upstream of exon 15 ASS. It is possible that this secondary competitor further weakens the exon 15 ASS thus enhancing the effects of variant chr8:g.87618576G>A.

Next, using OGI-081 as a true positive case, we tested whether splicing prediction algorithms could be used to prioritize candidate non-coding splicing altering variants, circumventing the need for RNA-seq analysis. We annotated the 3,268 rare variants with allelic pairs identified in OGI-081 with two splicing prediction programs. (i). Alamut Batch that makes its prediction by the combined

calculations of the same splicing predictions algorithms as Alamut visual but is capable of calculating the effects of multiple variants. (ii). SpliceAI, a deep neural network tool, to predict splice junctions from pre-mRNA transcript sequence<sup>18</sup>. Alamut batch calculated a high probability for altering splicing for 532 variants in 315 genes (Table S10). Although variant chr8:g.87618576G>A, the novel pathogenic variant identified in this study, was predicted by Alamut Batch to strongly activate a cryptic donor site the large number of additional candidate variants make this tool too cumbersome for identification of candidate non-coding pathogenic variants. For SpliceAI, to identify synonymous exonic, near intronic, and deep intronic variants predicted to affect splicing at a validation rate of 40% the authors used  $\Delta$  Score greater than or equal to 0.2, 0.2, and 0.5 respectively. Out of the variants segregating in OGI-081 only eight had scores  $0.2 < 0.5$  and only one, variant Chr9:g.86536129C>T, received a  $\Delta$  Score  $> 0.5$  (Table S11). Variant chr8:g.87618576G>A, the novel pathogenic variant identified in this study as activating a cryptic donor splice site, was calculated by SpliceAI to have a donor gain  $\Delta$  Score of 0.3 well below the 0.5 cutoff for deep intronic variants. Thus, had we used SpliceAI splicing predictions as a filter to identify potential causal variants for functional validations, variant chr8:g.87618576G>A would have been overlooked. The ASS of exon 14b was not identified by either algorithm and therefore could not have been used to highlight variant chr8:g.87618576G>A as a more plausible pathogenic variant.

## Discussion

We present here an unbiased approach based on the combination of WGS and RNA-seq data to identify and functionally validate pathogenic non-coding variants without the use of large datasets. We show that *ex vivo* models, such as iPSC derived ROs, can serve as a surrogate source of a patient's own retinal tissue for RNA and protein analyses. IRDs are currently at the focus of gene therapy advances and several clinical trials are underway, including a trial for *CNGB3* gene augmentation therapy<sup>6</sup>. This work was aimed at expanding the number of patients eligible for clinical trials and forthcoming therapies. Indeed, our findings here make the two affected siblings of OGI-081 eligible to participate in ongoing clinical trials for *CNGB3* gene therapy. Our approach is applicable to any inherited disease, both WGS and RNA-seq techniques are commercially available, gold standards are being established and the analysis tools are readily accessible<sup>47,48,82,49–55,81</sup>. *Ex vivo* organoid models are being developed for a multitude of tissues including brain<sup>83,84</sup>, kidney<sup>85</sup>, liver<sup>86,87</sup> and lung<sup>88</sup>.

Non-coding variants present a challenge for a correct genetic diagnosis that is imperative for a successful genetic therapy. The combination of WGS and RNA-seq methodologies allows us to both detect non-coding variants and evaluate their functionality throughout the genome. Indeed, a similar approach has already been successfully employed to diagnose diseases where RNA could be harvested from biopsies of disease-relevant tissue<sup>19,20</sup>. These studies relied on the availability of large control datasets of RNA-seq samples from unaffected

individuals and/or a large cohort of patients<sup>19,20</sup>. Our work shows that the correct diagnosis of non-coding variants is possible without reliance on such resources. WGS analysis of all five members of OGI-081 and segregation analysis of the variants within the family narrowed down the search from tens of thousands of variants to a few hundred with allelic pairs. We then used RNA-seq analysis comparing two affected siblings to an unaffected one as an orthogonal approach to identify genes with altered splicing or expression in disease. Thus identifying the deep intronic variant chr8:g.87618576G>A as a novel pathogenic variant in the *CNGB3* gene. The iPSC derived ROs served both as a source of disease relevant transcriptome and as a system for functional validation of the truncated proteins. In future studies, for families with a single patient the parents may serve as control samples, so that each parent controls for the effect of the allele inherited from the other parent making our approach applicable even for ultra-rare diseases.

Once the deep intronic variant was detected and validated we were able to use that prior knowledge to identify additional factors that may have contributed to the inclusion of exon 14b such as the availability of the cryptic acceptor site of exon 14b and the comparative weakness of the exon 15 acceptor site. Such complex dependencies are a prime example as to why sequence based predictions of splicing patterns are hard to compute. Still, several splicing predictors in the Alamut Visual software were able to detect the increase in the splicing probability of the cryptic donor site as a result of variant chr8:g.87618576G>A. This prompted us to test whether such splicing predictors can be used as preliminary

filters to identify candidate pathogenic variants for “gene by gene” validation methods, circumventing the need for RNA-seq analysis of ROs. We found that the more established approach represented by the Alamut Batch method of combining the calculations of several splicing predictors that are designed to identify known splicing motifs yielded too many candidates for gene by gene validation. In contrast, the more recent approach of deep neuronal networks algorithms, represented by SpliceAI, failed to assign high probability to the true positive variant chr8:g.87618576G>A. Still, in cases where some prior knowledge can help prioritize variants or highlight ones with lower than expected scores these methods may yet be helpful. In cases where no prior knowledge can help prioritize candidate variants, such as in patients where both pathogenic alleles are non-coding, and especially in cases where a cell type relevant for functional validation is not available, the approach established here is preferable.

## Appendices

### Differential gene expression analysis

As mentioned above, differential gene expression analysis was less informative in the OGI-081 datasets. We compared gene expression levels from each of the affected siblings to that of the unaffected sibling (Table S9). We found 401 genes to be consistently down regulated, of which 27 were Y linked as expected given that the two affected siblings are females while the unaffected sibling is a male. We excluded these Y linked genes from further analysis. Tools are not currently available to filter out non-Y linked genes that may be differentially expressed



between the sexes under normal conditions in ROs. Of the remaining 374 down regulated genes, 29 also contained allelic variant pairs (Table S3). In addition, we found 1120 genes to be consistently up regulated between the two affected siblings and the unaffected sibling (Table S9). Of the up regulated genes, 15 also contained allelic variant pairs (Table S3). None of the 44 differentially expressed genes with allelic variant pairs are reported in RetNet as IRD genes.

## Supplemental Data

Supplemental data includes two figures and 11 tables.

## Acknowledgments

The authors would like to thank the OGI-081 family for their participation in this study. We thank the members of the Ocular Genomics Institute Genomics Core facility for their assistance with sequencing analyses. We would like to thank Beryl Cumming for help generating the Sashimi plot in figure 2. This work was supported by grants from the National Eye Institute [R01EY012910 (EAP), R01EY026904 (KMB/EAP) and P30EY014104 (MEEI core support)], and the Foundation Fighting Blindness (EGI-GE-1218-0753-UCSD, KMB/EAP). DMG was supported by Foundation Fighting Blindness (BR-GE-1213-0632-UWI), Sandra Lemke Trout Chair in Eye Research, RRF Emmett A Humble Distinguished Directorship, McPherson Eye Research Institute, Research to Prevent Blindness. We acknowledge the Genotype-Tissue Expression (GTEx) Project that was supported by the Common Fund of the Office of the Director of the National Institutes of Health, and by NCI, NHGRI, NHLBI, NIDA, NIMH, and

NINDS. We acknowledge the ENCODE Consortium and the Thomas Gingeras, CSHL production lab for the use of skin RNA-seq samples ENCSR551NII, ENCSR991HIR, ENCSR460YCS and ENCSR321PGV.

## Declaration of Interests

The authors declare no competing interests.

## Web Resources

ENCODE <https://www.encodeproject.org/experiments/ENCSR551NII/>

ExAC <http://exac.broadinstitute.org/>

gnomAD <http://gnomad.broadinstitute.org/>

GTEx Portal <https://gtexportal.org/home/>

Picard tools <http://broadinstitute.github.io/picard/>

RetNet <http://www.sph.uth.tmc.edu/RetNet/>

## Accession Numbers

The accession numbers for the RNAseq samples reported in this paper (BioProject: PRJNA564377) are:

SRA:SRR10082823

SRA:SRR10082822

SRA:SRR10082821

566 SRA:SRR10082828

567 SRA:SRR10082829

568 SRA:SRR10082824

569 SRA:SRR10082830

570 SRA:SRR10082827

571 SRA:SRR10082826

572 SRA:SRR10082825

573 SRA:SRR10082820

574

## 575 References

576 1. Sahel, J.A., Marazova, K., and Audo, I. (2015). Clinical characteristics and  
577 current therapies for inherited retinal degenerations. Cold Spring Harb. Perspect.  
578 Med.

579 2. Maguire, A.M., Simonelli, F., Pierce, E.A., Pugh, E.N., Mingozzi, F., Bennicelli,  
580 J., Banfi, S., Marshall, K.A., Testa, F., Surace, E.M., et al. (2008). Safety and  
581 efficacy of gene transfer for Leber's congenital amaurosis. N. Engl. J. Med. 358,  
582 2240–2248.

583 3. Hauswirth, W.W., Aleman, T.S., Kaushal, S., Cideciyan, A. V., Schwartz, S.B.,  
584 Wang, L., Conlon, T.J., Boye, S.L., Flotte, T.R., Byrne, B.J., et al. (2008).  
585 Treatment of Leber congenital amaurosis due to RPE65 mutations by ocular  
586 subretinal injection of adeno-associated virus gene vector: Short-term results of a

587 phase I trial. *Hum. Gene Ther.* 19, 979–990.

588 4. Bainbridge, J.W.B., Smith, A.J., Barker, S.S., Robbie, S., Henderson, R.,  
589 Balaggan, K., Viswanathan, A., Holder, G.E., Stockman, A., Tyler, N., et al.  
590 (2008). Effect of gene therapy on visual function in Leber’s congenital amaurosis.  
591 *N. Engl. J. Med.* 358, 2231–2239.

592 5. Kannabiran, C., and Mariappan, I. (2018). Therapeutic avenues for hereditary  
593 forms of retinal blindness. *J. Genet.* 97, 341–352.

594 6. Moore, N.A., Morral, N., Ciulla, T.A., and Bracha, P. (2018). Gene therapy for  
595 inherited retinal and optic nerve degenerations. *Expert Opin. Biol. Ther.*

596 7. Scholl, H.P.N., Strauss, R.W., Singh, M.S., Dalkara, D., Roska, B., Picaud, S.,  
597 and Sahel, J.A. (2016). Emerging therapies for inherited retinal degeneration.  
598 *Sci. Transl. Med.*

599 8. Lek, M., Karczewski, K.J., Minikel, E. V., Samocha, K.E., Banks, E., Fennell,  
600 T., O’Donnell-Luria, A.H., Ware, J.S., Hill, A.J., Cummings, B.B., et al. (2016).  
601 Analysis of protein-coding genetic variation in 60,706 humans. *Nature*.

602 9. Karczewski, K.J., Francioli, L.C., Tiao, G., Cummings, B.B., Alföldi, J., Wang,  
603 Q., Collins, R.L., Laricchia, K.M., Ganna, A., Birnbaum, D.P., et al. (2019).  
604 Variation across 141,456 human exomes and genomes reveals the spectrum of  
605 loss-of-function intolerance across human protein-coding genes. *BioRxiv* 531210.

606 10. Vaz-Drago, R., Custódio, N., and Carmo-Fonseca, M. (2017). Deep intronic  
607 mutations and human disease. *Hum. Genet.* 136, 1093–1111.

608 11. Zhang, F., and Lupski, J.R. (2015). Non-coding genetic variants in human

609 disease: Figure 1. *Hum. Mol. Genet.* 24, R102–R110.

610 12. Khurana, E., Fu, Y., Chakravarty, D., Demichelis, F., Rubin, M.A., and  
611 Gerstein, M. (2016). Role of non-coding sequence variants in cancer. *Nat. Rev.*  
612 *Genet.* 17, 93–108.

613 13. Gloss, B.S., and Dinger, M.E. (2018). Realizing the significance of noncoding  
614 functionality in clinical genomics. *Exp. Mol. Med.*

615 14. Anna, A., and Monika, G. (2018). Splicing mutations in human genetic  
616 disorders: examples, detection, and confirmation.

617 15. Ohno, K., Takeda, J.-I.I., and Masuda, A. (2018). Rules and tools to predict  
618 the splicing effects of exonic and intronic mutations.

619 16. Cheng, J., Nguyen, T.Y.D., Cygan, K.J., Celik, M.H., Fairbrother, W.G.,  
620 Avsec, Z., and Gagneur, J. (2019). MMSplice: modular modeling improves the  
621 predictions of genetic variant effects on splicing. *Genome Biol.* 20, 48.

622 17. Jagadeesh, K.A., Paggi, J.M., Ye, J.S., Stenson, P.D., Cooper, D.N.,  
623 Bernstein, J.A., and Bejerano, G. (2018). S-CAP extends clinical-grade  
624 pathogenicity prediction to genetic variants that affect RNA splicing. *BioRxiv*.

625 18. Jaganathan, K., Kyriazopoulou Panagiotopoulou, S., McRae, J.F., Darbandi,  
626 S.F., Knowles, D., Li, Y.I., Kosmicki, J.A., Arbelaez, J., Cui, W., Schwartz, G.B.,  
627 et al. (2019). Predicting Splicing from Primary Sequence with Deep Learning.  
628 *Cell* 176, 535-548.e24.

629 19. Evrony, G.D., Cordero, D.R., Shen, J., Partlow, J.N., Yu, T.W., Rodin, R.E.,  
630 Hill, R.S., Coulter, M.E., Lam, A.T.N., Jayaraman, D., et al. (2017). Integrated

- genome and transcriptome sequencing identifies a noncoding mutation in the
- genome replication factor DONSON as the cause of microcephaly-micromelia
- syndrome. *Genome Res.*
20. Cummings, B.B., Marshall, J.L., Tukiainen, T., Lek, M., Donkervoort, S.,
- Foley, A.R., Bolduc, V., Waddell, L.B., Sandaradura, S.A., O'Grady, G.L., et al.
- (2017). Improving genetic diagnosis in Mendelian disease with transcriptome
- sequencing. *Sci. Transl. Med.*
21. Lonsdale, J., Thomas, J., Salvatore, M., Phillips, R., Lo, E., Shad, S., Hasz,
- R., Walters, G., Garcia, F., Young, N., et al. (2013). The Genotype-Tissue
- Expression (GTEx) project. *Nat. Genet.*
22. Ratnapriya, R., Sosina, O.A., Starostik, M.R., Kwicklis, M., Kapphahn, R.J.,
- Fritsche, L.G., Walton, A., Arvanitis, M., Gieser, L., Pietraszkiewicz, A., et al.
- (2019). Retinal transcriptome and eQTL analyses identify genes associated with
- age-related macular degeneration. *Nat. Genet.*
23. Aguet, F., Brown, A.A., Castel, S.E., Davis, J.R., He, Y., Jo, B., Mohammadi,
- P., Park, Y.S., Parsana, P., Segrè, A. V., et al. (2017). Genetic effects on gene
- expression across human tissues. *Nature.*
24. Danino, Y.M., Even, D., Ideses, D., and Juven-Gershon, T. (2015). The core
- promoter: At the heart of gene expression. *Biochim. Biophys. Acta - Gene Regul.*
- Mech.* **1849**, 1116–1131.
25. Rickels, R., and Shilatifard, A. (2018). Enhancer Logic and Mechanics in
- Development and Disease. *Trends Cell Biol.* **28**, 608–630.

26. Herzel, L., Ottoz, D.S.M., Alpert, T., and Neugebauer, K.M. (2017). Splicing and transcription touch base: co-transcriptional spliceosome assembly and function. *Nat. Rev. Mol. Cell Biol.* 18, 637–650.
27. Ramanouskaya, T. V., and Grinev, V. V. (2017). The determinants of alternative RNA splicing in human cells. *Mol. Genet. Genomics* 292, 1175–1195.
28. Gonorazky, H., Liang, M., Cummings, B., Lek, M., Micallef, J., Hawkins, C., Basran, R., Cohn, R., Wilson, M.D., MacArthur, D., et al. (2016). RNAseq analysis for the diagnosis of muscular dystrophy. *Ann. Clin. Transl. Neurol.* 3, 55–60.
29. Gonorazky, H.D., Naumenko, S., Ramani, A.K., Nelakuditi, V., Mashouri, P., Wang, P., Kao, D., Ohri, K., Viththiyapaskaran, S., Tarnopolsky, M.A., et al. (2019). Expanding the Boundaries of RNA Sequencing as a Diagnostic Tool for Rare Mendelian Disease. *Am. J. Hum. Genet.* 104, 466–483.
30. Capowski, E.E., Samimi, K., Mayerl, S.J., Phillips, M.J., Pinilla, I., Howden, S.E., Saha, J., Jansen, A.D., Edwards, K.L., Jager, L.D., et al. (2019). Reproducibility and staging of 3D human retinal organoids across multiple pluripotent stem cell lines. *Development* 146, dev171686.
31. Gonzalez-Cordero, A., Kruczek, K., Naeem, A., Fernando, M., Kloc, M., Ribeiro, J., Goh, D., Duran, Y., Blackford, S.J.I., Abelleira-Hervas, L., et al. (2017). Recapitulation of Human Retinal Development from Human Pluripotent Stem Cells Generates Transplantable Populations of Cone Photoreceptors. *Stem Cell Reports*.

- 675 32. Meyer, J.S., Shearer, R.L., Capowski, E.E., Wright, L.S., Wallace, K.A.,  
676 McMillan, E.L., Zhang, S.C., and Gamm, D.M. (2009). Modeling early retinal  
677 development with human embryonic and induced pluripotent stem cells. Proc.  
678 Natl. Acad. Sci. U. S. A.
- 679 33. Meyer, J.S., Howden, S.E., Wallace, K.A., Verhoeven, A.D., Wright, L.S.,  
680 Capowski, E.E., Pinilla, I., Martin, J.M., Tian, S., Stewart, R., et al. (2011). Optic  
681 vesicle-like structures derived from human pluripotent stem cells facilitate a  
682 customized approach to retinal disease treatment. Stem Cells.
- 683 34. Nakano, T., Ando, S., Takata, N., Kawada, M., Muguruma, K., Sekiguchi, K.,  
684 Saito, K., Yonemura, S., Eiraku, M., and Sasai, Y. (2012). Self-formation of optic  
685 cups and storable stratified neural retina from human ESCs. Cell Stem Cell.
- 686 35. Phillips, M.J., Wallace, K.A., Dickerson, S.J., Miller, M.J., Verhoeven, A.D.,  
687 Martin, J.M., Wright, L.S., Shen, W., Capowski, E.E., Percin, E.F., et al. (2012).  
688 Blood-derived human iPS cells generate optic vesicle-like structures with the  
689 capacity to form retinal laminae and develop synapses. Invest. Ophthalmol. Vis.  
690 Sci.
- 691 36. Reichman, S., Terray, A., Slembrouck, A., Nanteau, C., Orioux, G., Habeler,  
692 W., Nandrot, E.F., Sahel, J.A., Monville, C., and Goureau, O. (2014). From  
693 confluent human iPS cells to self-forming neural retina and retinal pigmented  
694 epithelium. Proc. Natl. Acad. Sci. U. S. A.
- 695 37. Wahlin, K.J., Maruotti, J.A., Sripathi, S.R., Ball, J., Angueyra, J.M., Kim, C.,  
696 Grebe, R., Li, W., Jones, B.W., and Zack, D.J. (2017). Photoreceptor Outer



Segment-like Structures in Long-Term 3D Retinas from Human Pluripotent Stem Cells. *Sci. Rep.*

38. Zhong, X., Gutierrez, C., Xue, T., Hampton, C., Vergara, M.N., Cao, L.H., Peters, A., Park, T.S., Zambidis, E.T., Meyer, J.S., et al. (2014). Generation of three-dimensional retinal tissue with functional photoreceptors from human iPSCs. *Nat. Commun.*

39. Cora, V., Haderspeck, J., Antkowiak, L., Mattheus, U., Neckel, P.H., Mack, A.F., Bolz, S., Ueffing, M., Pashkovskaia, N., Achberger, K., et al. (2019). A Cleared View on Retinal Organoids. *Cells* 8, 391.

40. Kim, S., Lowe, A., Dharmat, R., Lee, S., Owen, L.A., Wang, J., Shakoob, A., Li, Y., Morgan, D.J., Hejazi, A.A., et al. (2019). Generation, transcriptome profiling, and functional validation of cone-rich human retinal organoids. *Proc. Natl. Acad. Sci.* 116, 10824–10833.

41. Capowski, E.E., Samimi, K., Mayerl, S.J., Phillips, M.J., Pinilla, I., Howden, S.E., Saha, J., Jansen, A.D., Edwards, K.L., Jager, L.D., et al. (2018). Reproducibility and staging of 3D human retinal organoids across multiple pluripotent stem cell lines. *Development* 146, dev171686.

42. Consugar, M.B., Navarro-Gomez, D., Place, E.M., Bujakowska, K.M., Sousa, M.E., Fonseca-Kelly, Z.D., Taub, D.G., Janessian, M., Wang, D.Y., Au, E.D., et al. (2015). Panel-based genetic diagnostic testing for inherited eye diseases is highly accurate and reproducible, and more sensitive for variant detection, than exome sequencing. *Genet. Med.* 17, 253–261.

719 43. Falk, M.J., Zhang, Q., Nakamaru-Ogiso, E., Kannabiran, C., Fonseca-Kelly,  
720 Z., Chakarova, C., Audo, I., MacKay, D.S., Zeitz, C., Borman, A.D., et al. (2012).  
721 NMNAT1 mutations cause Leber congenital amaurosis. *Nat. Genet.*

722 44. Hardwick, S.A., Chen, W.Y., Wong, T., Deveson, I.W., Blackburn, J.,  
723 Andersen, S.B., Nielsen, L.K., Mattick, J.S., and Mercer, T.R. (2016). Spliced  
724 synthetic genes as internal controls in RNA sequencing experiments. *Nat.*  
725 *Methods* 13, 792–798.

726 45. McLaren, W., Gil, L., Hunt, S.E., Riat, H.S., Ritchie, G.R.S., Thormann, A.,  
727 Flicek, P., and Cunningham, F. (2016). The Ensembl Variant Effect Predictor.  
728 *Genome Biol.*

729 46. Handsaker, R.E., Van Doren, V., Berman, J.R., Genovese, G., Kashin, S.,  
730 Boettger, L.M., and Mccarroll, S.A. (2015). Large multiallelic copy number  
731 variations in humans. *Nat. Genet.*

732 47. Ewels, P., Magnusson, M., Lundin, S., and Käller, M. (2016). MultiQC:  
733 summarize analysis results for multiple tools and samples in a single report.  
734 *Bioinformatics* 32, 3047–3048.

735 48. Dobin, A., Davis, C.A., Schlesinger, F., Drenkow, J., Zaleski, C., Jha, S.,  
736 Batut, P., Chaisson, M., and Gingeras, T.R. (2013). STAR: ultrafast universal  
737 RNA-seq aligner. *Bioinformatics* 29, 15–21.

738 49. Liao, Y., Smyth, G.K., and Shi, W. (2014). featureCounts: an efficient general  
739 purpose program for assigning sequence reads to genomic features.  
740 *Bioinformatics* 30, 923–930.

50. Wong, T., Deveson, I.W., Hardwick, S.A., and Mercer, T.R. (2017). ANAQUIN: a software toolkit for the analysis of spike-in controls for next generation sequencing. *Bioinformatics* 33, 1723–1724.
51. Wu, W., Zong, J., Wei, N., Cheng, J., Zhou, X., Cheng, Y., Chen, D., Guo, Q., Zhang, B., and Feng, Y. (2018). CASH: a constructing comprehensive splice site method for detecting alternative splicing events. *Brief. Bioinform.* 19, 905–917.
52. Vaquero-Garcia, J., Barrera, A., Gazzara, M.R., González-Vallinas, J., Lahens, N.F., Hogenesch, J.B., Lynch, K.W., and Barash, Y. (2016). A new view of transcriptome complexity and regulation through the lens of local splicing variations. *Elife* 5, e11752.
53. Robinson, M.D., McCarthy, D.J., and Smyth, G.K. (2010). edgeR: a Bioconductor package for differential expression analysis of digital gene expression data. *Bioinformatics* 26, 139–140.
54. Wang, L., Wang, S., and Li, W. (2012). RSeQC: quality control of RNA-seq experiments. *Bioinformatics* 28, 2184–2185.
55. Bray, N.L., Pimentel, H., Melsted, P., and Pachter, L. (2016). Near-optimal probabilistic RNA-seq quantification. *Nat. Biotechnol.* 34, 525–527.
56. Farkas, M.H., Grant, G.R., White, J. a, Sousa, M.E., Consugar, M.B., Pierce, E. a, and Genomics, B. (2013). Transcriptome analyses of the human retina identify unprecedented transcript diversity and 3.5 Mb of novel transcribed sequence via significant alternative splicing and novel genes. *BMC Genomics* 14, 486.

- 763 57. Mossman, S.S., Bronstein, A.M., Gresty, M.A., Kendall, B., and Rudge, P.  
764 (1990). Convergence nystagmus associated with Arnold-Chiari malformation.  
765 Arch. Neurol. 47, 357–359.
- 766 58. Milhorat, T.H., Chou, M.W., Trinidad, E.M., Kula, R.W., Mandell, M., Wolpert,  
767 C., and Speer, M.C. (1999). Chiari I malformation redefined: clinical and  
768 radiographic findings for 364 symptomatic patients. Neurosurgery 44, 1005–  
769 1017.
- 770 59. Urbizu, A., Toma, C., Poca, M.A., Sahuquillo, J., Cuenca-León, E., Cormand,  
771 B., and Macaya, A. (2013). Chiari malformation type I: a case-control association  
772 study of 58 developmental genes. PLoS One 8, e57241.
- 773 60. Shaikh, A., and Ghasia, F. (2015). Neuro-ophthalmology of type Chiari  
774 malformation. Expert Rev Ophtalmol 10, 351–357.
- 775 61. Ray, C., Nagy, L., and Mobley, J. (2014). Familial aggregation of chiari  
776 malformation: presentation, pedigree, and review of the literature. Turk.  
777 Neurosurg. 26, 315–320.
- 778 62. Yuan, X.X., Li, Y., Sha, S.F., Sun, W.X., Qiu, Y., Liu, Z., Zhu, W.G., and Zhu,  
779 Z.Z. (2017). [Genetic analysis of posterior cranial fossa morphology in families of  
780 Chiari malformation type I ]. Zhonghua Yi Xue Za Zhi 97, 1140–1144.
- 781 63. Sarnat, H.B. (2018). Cerebellar networks and neuropathology of cerebellar  
782 developmental disorders (Elsevier).
- 783 64. Merello, E., Tattini, L., Magi, A., Accogli, A., Piatelli, G., Pavanello, M.,  
784 Tortora, D., Cama, A., Kibar, Z., Capra, V., et al. (2017). Exome sequencing of

785 two Italian pedigrees with non-isolated Chiari malformation type I reveals  
786 candidate genes for cranio-facial development. *Eur. J. Hum. Genet.* 25, 952–959.  
787 65. Solis-Moruno, M., de Manuel, M., Hernandez-Rodriguez, J., Fonsere, C.,  
788 Gomara-Castaño, A., Valsera-Naranjo, C., Crailsheim, D., Navarro, A., Llorente,  
789 M., Riera, L., et al. (2017). Potential damaging mutation in LRP5 from genome  
790 sequencing of the first reported chimpanzee with the Chiari malformation. *Sci.*  
791 *Rep.* 7, 15224.  
792 66. Wiszniewski, W., Lewis, R.A., and Lupski, J.R. (2007). Achromatopsia: the  
793 CNGB3 p.T383fsX mutation results from a founder effect and is responsible for  
794 the visual phenotype in the original report of uniparental disomy 14. *Hum. Genet.*  
795 121, 433–439.  
796 67. Nishiguchi, K.M., Sandberg, M.A., Gorji, N., Berson, E.L., and Dryja, T.P.  
797 (2005). Cone cGMP-gated channel mutations and clinical findings in patients with  
798 achromatopsia, macular degeneration, and other hereditary cone diseases. *Hum.*  
799 *Mutat.* 25, 248–258.  
800 68. Kohl, S. (2000). Mutations in the CNGB3 gene encoding the beta-subunit of  
801 the cone photoreceptor cGMP-gated channel are responsible for achromatopsia  
802 (ACHM3) linked to chromosome 8q21. *Hum. Mol. Genet.* 9, 2107–2116.  
803 69. Maguire, J., McKibbin, M., Khan, K., Kohl, S., Ali, M., and McKeefry, D.  
804 (2018). CNGB3 mutations cause severe rod dysfunction. *Ophthalmic Genet.* 39,  
805 108–114.  
806 70. Mayer, A.K., Van Cauwenbergh, C., Rother, C., Baumann, B., Reuter, P., De

807 Baere, E., Wissinger, B., and Kohl, S. (2017). CNGB3 mutation spectrum  
808 including copy number variations in 552 achromatopsia patients. *Hum. Mutat.* 38,  
809 1579–1591.

810 71. Nishiguchi, K.M., and Rivolta, C. (2012). Genes associated with retinitis  
811 pigmentosa and allied diseases are frequently mutated in the general population.  
812 *PLoS One* 7,.

813 72. Baralle, F.E., and Giudice, J. (2017). Alternative splicing as a regulator of  
814 development and tissue identity. *Nat. Rev. Mol. Cell Biol.* 18, 437–451.

815 73. Bush, S.J., Chen, L., Tovar-Corona, J.M., and Urrutia, A.O. (2017).  
816 Alternative splicing and the evolution of phenotypic novelty. *Philos. Trans. R.*  
817 *Soc. Lond. B. Biol. Sci.* 372,.

818 74. ENCODE Project, Bernstein, B.E., Birney, E., Dunham, I., Green, E.D.,  
819 Gunter, C., and Snyder, M. (2012). An integrated encyclopedia of DNA elements  
820 in the human genome. *Nature*.

821 75. Davis, C.A., Hitz, B.C., Sloan, C.A., Chan, E.T., Davidson, J.M., Gabdank, I.,  
822 Hilton, J.A., Jain, K., Baymuradov, U.K., Narayanan, A.K., et al. (2018). The  
823 Encyclopedia of DNA elements (ENCODE): data portal update. *Nucleic Acids*  
824 *Res.* 46, D794–D801.

825 76. Bönigk, W., Altenhofen, W., Müller, F., Dose, A., Illing, M., Molday, R.S., and  
826 Kaupp, U.B. (1993). Rod and cone photoreceptor cells express distinct genes for  
827 cGMP-gated channels. *Neuron* 10, 865–877.

828 77. Matveev, A. V, Quiambao, A.B., Browning Fitzgerald, J., and Ding, X.-Q.

- (2008). Native cone photoreceptor cyclic nucleotide-gated channel is a heterotetrameric complex comprising both CNGA3 and CNGB3: a study using the cone-dominant retina of Nrl<sup>-/-</sup> mice. *J. Neurochem.* 106, 2042–2055.
78. Shapiro, M.B., and Senapathy, P. (1987). RNA splice junctions of different classes of eukaryotes: sequence statistics and functional implications in gene expression. *Nucleic Acids Res.* 15, 7155–7174.
79. Yeo, G., and Burge, C.B. (2004). Maximum entropy modeling of short sequence motifs with applications to RNA splicing signals. *J. Comput. Biol.* 11, 377–394.
80. Reese, M.G., Eeckman, F.H., Kulp, D., and Haussler, D. (1997). Improved Splice Site Detection in Genie. *J. Comput. Biol.* 4, 311–323.
81. Langmead, B., and Salzberg, S.L. (2012). Fast gapped-read alignment with Bowtie 2. *Nat. Methods* 9, 357–359.
82. Li, H., Handsaker, B., Wysoker, A., Fennell, T., Ruan, J., Homer, N., Marth, G., Abecasis, G., Durbin, R., and 1000 Genome Project Data Processing Subgroup, 1000 Genome Project Data Processing (2009). The Sequence Alignment/Map format and SAMtools. *Bioinformatics* 25, 2078–2079.
83. Cosset, E., Locatelli, M., Marteyn, A., Lescuyer, P., Dall Antonia, F., Mor, F.M., Preynat-Seauve, O., Stoppini, L., and Tieng, V. (2019). Human Neural Organoids for Studying Brain Cancer and Neurodegenerative Diseases. *J. Vis. Exp.*
84. Gopalakrishnan, J. (2019). The Emergence of Stem Cell-Based Brain

851 Organoids: Trends and Challenges. *Bioessays* 41, e1900011.

852 85. Low, J.H., Li, P., Chew, E.G.Y., Zhou, B., Suzuki, K., Zhang, T., Lian, M.M.,  
853 Liu, M., Aizawa, E., Rodriguez Esteban, C., et al. (2019). Generation of Human  
854 PSC-Derived Kidney Organoids with Patterned Nephron Segments and a De  
855 Novo Vascular Network. *Cell Stem Cell*.

856 86. Prior, N., Inacio, P., and Huch, M. (2019). Liver organoids: from basic  
857 research to therapeutic applications. *Gut*.

858 87. Torresi, J., Tran, B.M., Christiansen, D., Earnest-Silveira, L., Schwab,  
859 R.H.M., and Vincan, E. (2019). HBV-related hepatocarcinogenesis: the role of  
860 signalling pathways and innovative ex vivo research models. *BMC Cancer* 19,  
861 707.

862 88. Strikoudis, A., Cieřlak, A., Loffredo, L., Chen, Y.W., Patel, N., Saqi, A.,  
863 Lederer, D.J., and Snoeck, H.W. (2019). Modeling of Fibrotic Lung Disease  
864 Using 3D Organoids Derived from Human Pluripotent Stem Cells. *Cell Rep*.  
865



## Figure Legends

### **Figure 1: Family OGI-081 variant segregation scheme and retinal**

**phenotypes.** A. The OGI-081 pedigree with variant segregation scheme. B.

Fundus (upper panel) and OCT image (lower panel) for the OGI-081-197 at age 8, area of retinal degeneration is indicated by the red bar.

### **Figure 2: RO differentiation.** A. Schema of the differentiation process and a

light microscopy image of a typical RO. Arrow head indicating photoreceptors,

scale bar = 100 microns. B-G. Immunocytochemistry on cryosections of ROs.

B&E. NR2E3 staining of rod nuclei (Green). C&F. Mature cones show staining of

cone opsins in the cone photoreceptor outer segments (Red). C. S opsin. F. ML

opsin. D&G. Overlay of rod and cone staining. All cones are stained with ARR3

(Purple). Scale bars = 20 microns.

### **Figure 3: Comparison of IRD gene expression and splice junctions.** Human

Normal Retina (HNR; N=3, gray), RO from the unaffected sibling (N=5, blue),

Skin-Sun Exposed (SSE; N=473, green) and Whole Blood (WB; N=407, red).

A&B Average TPM values of IRD genes. A. IRD genes are sorted by their

expression in HNR overlaid with RO, SSE or WB. B. Violin plot. C&D Number of

splice junctions detected by MAJIQ. C. All annotated genes. D. IRD genes.

### **Figure 4: Alternative splicing in the *NCALD* and *CNGB3* genes.** A. Venn

diagram of genes found to have alternative splicing events in OGI-081

comparison of affected vs. unaffected siblings and genes found to have

segregating allelic pairs (green). Alternative splicing analysis was conducted by

MAJIQ (blue) and CASH (red). B. Collapsed diagram of exons (black boxes) from all isoforms of the *NCALD* and *CNGB3* genes. DNA variants (red); MAJIQ (blue) and CASH (yellow) alternative splicing events (E). Events detected by MAJIQ are depicted as split reads arches. The event range detected by CASH is depicted by the left (L) and right (R) borders. Genomic locations of variants, junctions and event borders are given in table S6.

**Figure 5: Aberrant splicing of *CNGB3* in the affected vs. unaffected**

**siblings.** A. Sashimi plot presenting RNA-seq results showing a cryptic exon spliced into the isoform as a result of the intronic variant chr8:g.87618576G>A. The cryptic exon is only present in the affected sibling (lower panel, red) and not in the unaffected sibling (upper panel, blue). The splice junction between exon 14b and exon 15 is not represented by split reads in the Sashimi plot due to an alignment error (FigureS1). B. RT-PCR using primers from the canonical exon14 and exon 15. All three siblings express the normal size isoform lacking exon 14b (lower band). A larger abnormal band containing exon14b (upper band) is present in the two affected siblings Af1 and Af2 but not in the unaffected sibling (Un). Negative controls lacking RNA template in the RT reaction (NC1) and NC1 used as template for PCR amplification (NC2). Sanger sequencing of the larger band confirming the inclusion of exon 14b. C. Schematic representation of the protein domains in W.T *CNGB3* and the two mutant alleles found in the affected siblings of OGI-081.

**Figure 6: Mislocalization of the *CNGB3* truncated proteins.**

Immunocytochemical analysis of day 262 ROs from the heterozygous parent

911 OGI-081-200 (A-C) and an affected sibling OGI-081-197 (D-F). In the  
 912 heterozygote, both ML opsins (red) and CNGB3 (green) are localized to the  
 913 photoreceptor outer segments whereas in the affected sibling, CNGB3 localizes  
 914 to the photoreceptor inner segments. An exemplary photoreceptor outer segment  
 915 is indicated by the white brackets. Nuclei are counterstained with DAPI (blue).  
 916 Scale bars = 20 micron

917

**Table 1: Sample level alignment report and QC summary.** A high average

unique percentage alignment rate is reported.

SampleName	RawReads <sup>a</sup>	HQReads <sup>b</sup>	% UniqAligned <sup>c</sup>
OGI-081-197-1	159,976,749	129,671,633	87.73
OGI-081-197-2	256,399,765	234,701,223	90.52
OGI-081-197-3	166,237,226	155,442,261	88.88
OGI-081-198-1	167,327,080	145,058,230	88.66
OGI-081-198-2	197,037,935	179,026,100	89.13
OGI-081-198-3	191,485,904	177,663,416	90.15
OGI-081-340-1	175,199,604	156,566,678	91.01
OGI-081-340-2	227,928,431	216,526,830	89.53
OGI-081-340-3	137,096,260	129,192,437	90.47
OGI-081-340-4	151,572,341	140,982,711	90.59
OGI-081-340-5	164,908,758	154,550,198	99.66

<sup>a</sup> Raw reads count (RawReads), <sup>b</sup> Filtered high quality reads (HQReads), <sup>c</sup>

Percent of uniquely aligned reads (% UniqAligned).

**Table 2: Splicing junctions involved with the inclusion of exon14b.**

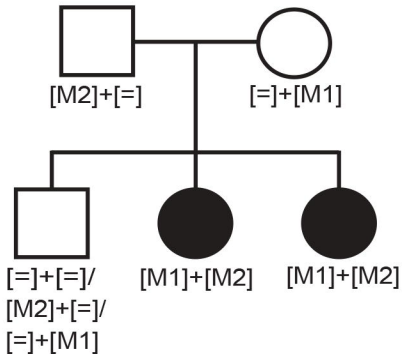
	Exon 14 Donor site	Exon 14b Acceptor site	Exon 14b Donor site		Exon 15 Acceptor site	
	Annotated	W.T	W.T	Variant	Annotated	W.T
NM_019098.4 <sup>a</sup>	c.1662	c.1663-2238	c.1663-2137	c.1663-2137C>T	c.1663	c.1663-54
SSF <sup>b</sup>	95.3	83.3	67.8	73.7	76.7	90.4
MaxEntScan <sup>c</sup>	10.5	4.8	0	4.8	6.1	8.7
NNSplice <sup>d</sup>	1	0.5	0	1	0.1	0.8

<sup>a</sup> The NM\_019098.4 isoform of CNGB3 is used to define the cDNA coordinates. <sup>b-</sup>

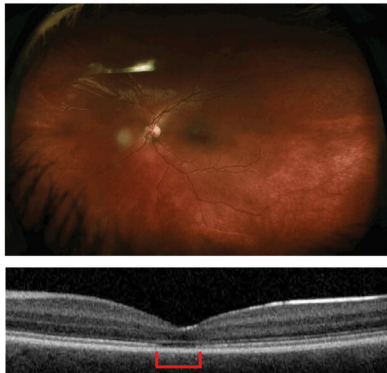
<sup>d</sup> Splicing prediction scores are given from the three algorithms, SSF,

MaxEntScan and NNSplice.

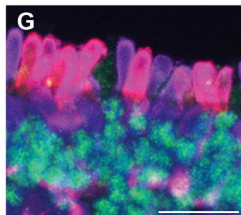
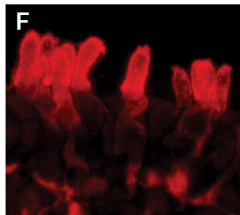
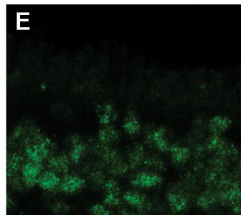
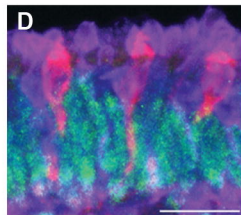
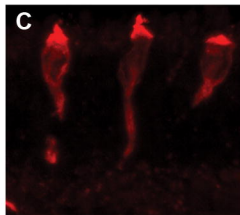
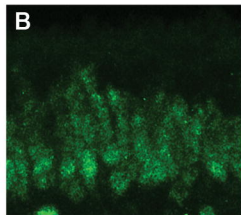
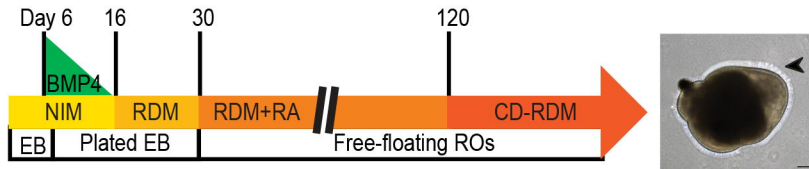
A.

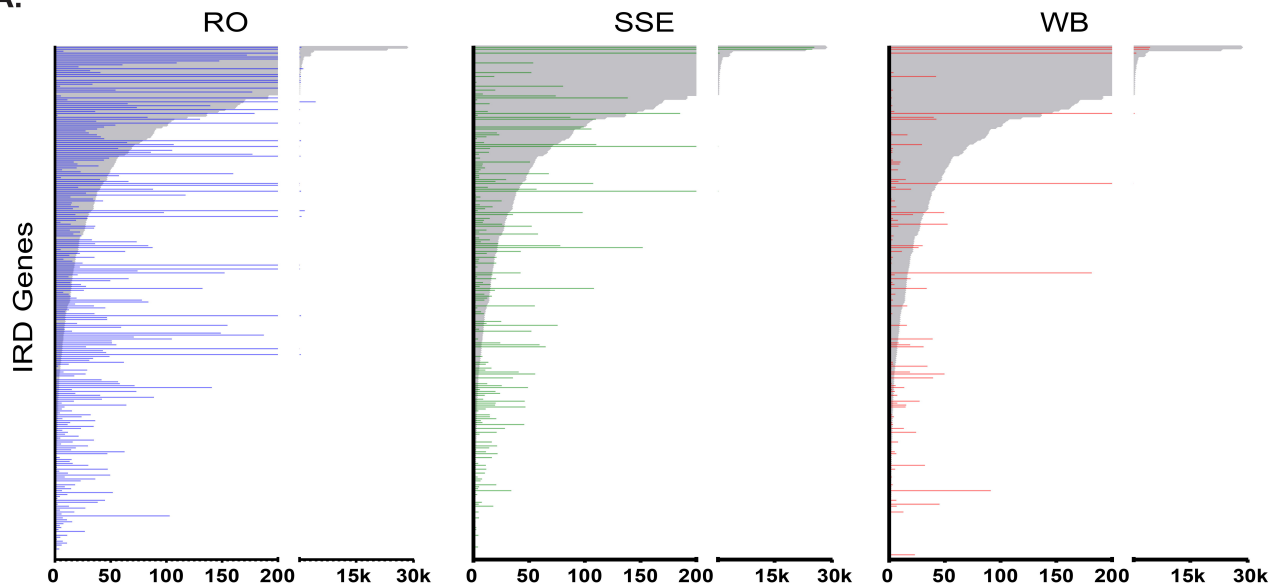
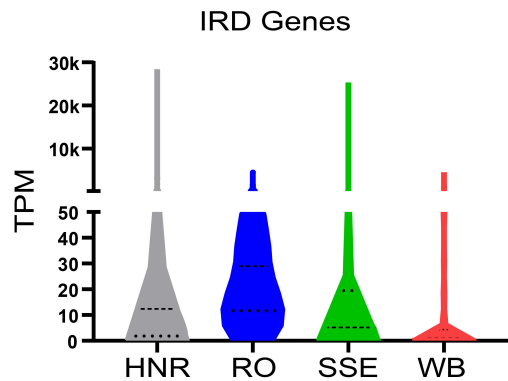
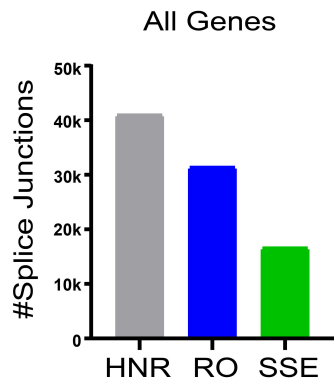
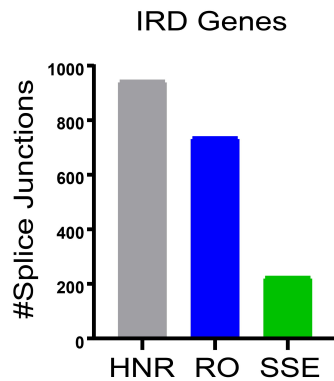


B.

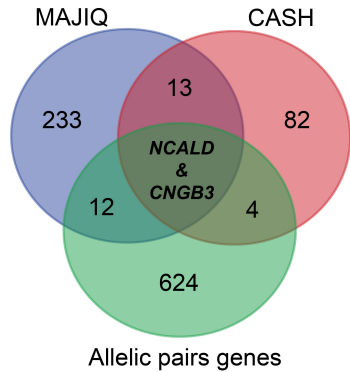


A.

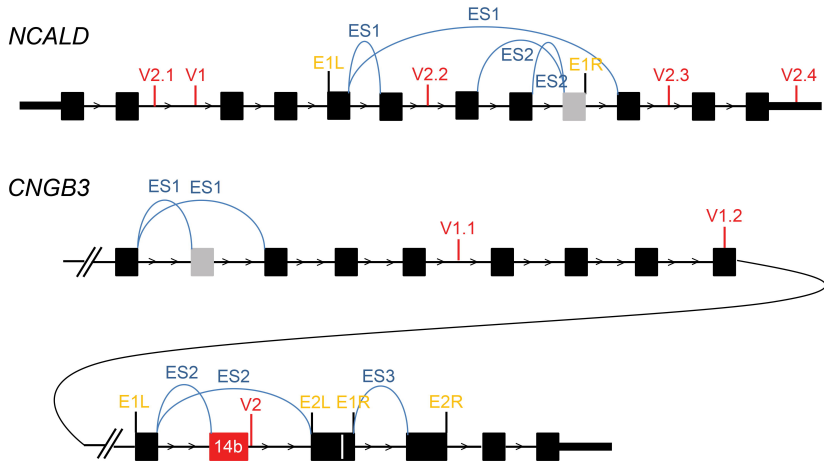


**A.****B.****C.****D.**

A.

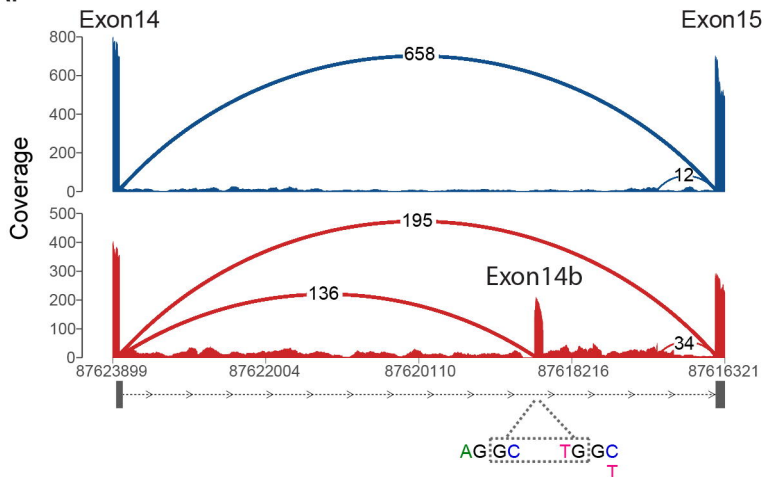


B.

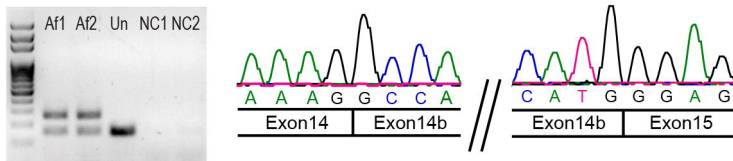




A.



B.



C.

